doi:10.20944/preprints202103.0295.v1

Research Article

Non- and Quasi-Equilibrium Multi-Phase Field Methods Coupled with CALPHAD Database for Rapid-Solidification Microstructural Evolution in Laser Powder Bet Additive Manufacturing Condition

Sukeharu Nomoto [1*], Masahito Segawa [2] and Makoto Watanabe [3]

[1] National Institute for Material Science; NOMOTO.Sukeharu@nims.go.jp
[2] ITOCHU Techno-Solutions Corporation; masahito.segawa@ctc-g.co.jp
[3] National Institute for Material Science; MAKOTO.Watanabe@nims.go.jp
* Correspondence: NOMOTO.Sukeharu@nims.go.jp

Abstract: Solidification microstructure is formed under high cooling rates and temperature gradients in powder-based additive manufacturing. In this study, a non-equilibrium multi-phase field method (MPFM), which was based on a finite interface dissipation model proposed by Steinbach *et. al*., coupled with a CALPHAD database was developed for a multicomponent Ni alloy. A quasi-equilibrium MPFM was also developed for comparison. Two-dimensional equiaxed microstructural evolution for the Ni (Bal.)–Al–Co–Cr–Mo–Ta–Ti–W–C alloy was performed at various cooling rates. The temperature–γ fraction profiles obtained under 10^5 K/s using non- and quasi-equilibrium MPFMs were in good agreement with each other. Over 10^6 K/s, the differences between non- and quasi-equilibrium methods grew as the cooling rate increased. The non-equilibrium solidification was strengthened over a cooling rate of 10^6 K/s. Columnar-solidification microstructural evolution was performed under cooling rates from 5×10^5 K/s to 1×10^7 K/s at various temperature gradient values under the constant interface velocity (0.1 m/s). The results showed that as the cooling rate increased, the cell space decreased in both methods, and the non-equilibrium MPFM agreed well with experimental measurements. Our results show that the non-equilibrium MPFM can simulate solidification microstructure in powder bed fusion additive manufacturing.

Keywords: additive manufacturing; rapid solidification; microstructural evolution; non-equilibrium; quasi-equilibrium; multi-phase field method; CALPHAD database; nickel alloy

1. Introduction

Additive manufacturing is used to produce complex three-dimensional machine parts by feeding alloy powder layer by layer. The powder layer surface is irradiated by a high-power laser, melted, and solidified in every feeding. This process is called laser powder bed fusion (LPBF). The mechanical properties of machine parts fabricated by LPBF often supersede those produced by conventional casting methods due to the unique solidification microstructure [1]. The short diameter (100 μm) and high moving speeds (0.1-1m/s orders) of the laser spot enable high cooling rates and temperature gradients around the melting pool. These conditions lead to the microstructure resulting in exceptional mechanical properties [2-4]. Many researchers have reported that the solidification microstructure obtained by LPBF was produced using cooling ranges from 10^4 K/s to 10^6 K/s and temperature gradients from 10^5 K/s to 10^7 K/s [5-7]. Rapid solidification is desired to design the LPBF process parameters to obtain precise microstructure. However, analyzing high-speed rapid solidification in LPBF is experimentally challenging. Therefore, numerical methodologies can help to unravel the mechanism of rapid solidification in LPBF.

Many FEM analyses have been performed to show the temporal temperature distributions around the moving laser spot [8-10]. Furthermore, CFD analyses have been performed to obtain not only the temperature distribution but also the fluid flow in the melt pool by considering the free surface affected by Marangoni convection. The macroscopic solidifications have been attempted by weak coupling with the temporal temperature distribution or by the VOF method in CFD analysis [11,12]. However, these numerical techniques do not provide information about microstructural evolution and cellular or dendric growths because constitutional cooling is not rigorously estimated due to its large-scale discretization for description of solute diffusion boundary layer. Moreover, cellular automaton applied to relatively short length scales provides cellular or dendritic growth, considering constitutional undercooling [13,14]. Recently, columnar-to-equiaxed transition analysis was successfully applied to rapid solidification conditions in LPBF. The multi-phase field method (MPFM) has been used along with weak coupling analyses, macroscopic thermal and/or fluid dynamics, and microstructural evolution [15-18]. Local equilibrium and quasi-equilibrium assumptions are usually assumed for cellular automaton or the MPFM [19], respectively. These assumptions could be applied to rapid solidification in LPBF [20].

The finite interface dissipation model for the phase-field method (PFM) was proposed by Steinbach *et. al*. [21,22]. This model permits the PFM to describe the non-equilibrium solute distribution with a new parameter called *permeability* at the interface region. By using this model, the MPFM has been extended to a multi-component system consisting of substitutional and interstitial elements in combination with a CALPHAD database. Recently, Karayagiz *et. al.* performed solidification microstructure analysis using the non-equilibrium, finite interface dissipation, and MPFM for a Ni–Nb binary system by weakly coupling with FEM thermal analysis in LPBF [23]. They found that the segregation coefficient value simulated by the non-equilibrium MPFM was close to the quasi-equilibrium MPFM as permeability value increasing.

So far, the literature on solidification microstructure evolution by the MPFM was usually studied in binary or ternary systems. In this study, we developed non- and quasi-equilibrium MPFMs coupled with a CALPHAD database for Ni alloy of engineering multi-component. Next, non- and quasi-equilibrium MPFMs were compared to equiaxed microstructure evolution simulations at various cooling rates. Finally, columnar microstructure evolutions performed by both MPFMs in the same steady interface under various cooling rates and temperature gradients were compared and discussed.

2. Model Description and Computational Procedure

2.1. Non- and Quasi-Equilibrium Multi-Phase Field Method

The finite interface dissipation model proposed by Steinbach and Zhang [22] was adapted to develop the non-equilibrium MPFM. This MPFM equation has the same structure as the conventional MPFM. The conventional MPFM equation is based on a quasi-equilibrium assumption that is defined by the parallel tangent law between Gibbs free energy curves varying with solute compositions of two or more phases according to the KKS model [24]. This restriction is not necessary for the non-equilibrium MPFM. The MPFM equation is described by using the double-obstacle potential for consistency as follows:

$$\frac{\partial \phi_\alpha}{\partial t} = \sum_{\beta=1}^{N} \frac{K_{\alpha\beta}}{N} \left\{ \sum_{k=1}^{N} \left[\left(\frac{\pi^2}{\delta^2} \phi_k + \nabla^2 \phi_k \right) \left(\sigma_{\beta k} - \sigma_{\alpha k} \right) \right] + \frac{2\pi}{\delta} \sqrt{\phi_\alpha \phi_\beta} \, \Delta G_{\alpha\beta} \right\} \qquad (1)$$

where $\emptyset_\alpha$, $\sigma_{\beta k}$, $K_{\alpha\beta}$, δ, and N are the phase order ($0 \leqq \emptyset_\alpha \leqq 1$), interface energy, interface mobility, interface width, and number of phases or grains constructing the interface, respectively. $\Delta G_{\alpha\beta}$ is the interface driving force between phases α and β. For non-equilibrium MPFM, it is expressed as

$$\Delta G_{\alpha\beta} = f_{\beta} - f_{\alpha} - \sum_{i=1}^{n-1}\sum_{\varsigma=1}^{N} \phi_{\varsigma}\, \tilde{\mu}_{\varsigma}^{i}\left(c_{\beta}^{i} - c_{\alpha}^{i}\right) \tag{2}$$

where f_α, f_β, c_α^i, c_β^i, $\tilde{\mu}_\zeta^i$ and n are the Gibbs free energy density of phases α and β, the molar fraction of element i in phases α and β, the diffuse potential that is the gradient of the Gibbs free energy tangent line for element i composition direction in phase ζ and number of (solute and solvent Ni) elements in the system, respectively. In the conventional MPFM, the diffuse potential values of all phases at a point at the interface become equal, $\tilde{\mu}_\gamma^i = \tilde{\mu}^i$. The driving force, $\Delta G_{\alpha\beta}$, is expressed as

$$\Delta G_{\alpha\beta} = f_{\beta} - f_{\alpha} - \sum_{i=1}^{n-1} \tilde{\mu}^{i}\left(c_{\beta}^{i} - c_{\alpha}^{i}\right) \tag{3}$$

The conventional MPFM driving force can be considered as a special case of the non-equilibrium MPFM.

The interface mobility correction is essential to precisely control interface motion. Interface mobility values were corrected according to the equation (16) of [25] and the equation (35) of [26] for quasi- and non-equilibrium MPFMs, respectively. The anti-trapping current was also implemented by the equation (29) of [26]. These equations were derived for the double-obstacle potential of the phase-field equation.

The evolution equations of solute compositions in the interface region were proposed by Zhang *et. al.* [25] as follows:

$$\dot{c}^{i} = \nabla\cdot\sum_{\alpha=1}^{N}\left[\phi_{\alpha}\sum_{j=1}^{n-1} D_{ij}^{\alpha}\,\nabla c_{\alpha}^{j}\right] + \sum_{\beta=1}^{N} P_{\alpha\beta}^{i}\phi_{\beta}\left(\tilde{\mu}_{\beta}^{i} - \tilde{\mu}_{\alpha}^{i}\right) - \sum_{\beta=1}^{N}\dot{\phi}_{\beta}\left(c_{\beta}^{i} - c_{\alpha}^{i}\right) \tag{3}$$

where D_{ij}^α is the diffusivity matrix in phase α. $P_{\alpha\beta}^i$ is a new parameter named interface permeability that acts as a strength partitioning solute element i between phases α and β. Eq. (4) is separated into two steps according to our previous study [27]:

$$\dot{c}^{i} = \nabla\cdot\sum_{\alpha=1}^{N}\left[\phi_{\alpha}\sum_{j=1}^{n-1} D_{ij}^{\alpha}\,\nabla c_{\alpha}^{j}\right], \tag{5}$$

$$\dot{c}_{\alpha}^{i} = \sum_{\beta=1}^{N} P_{\alpha\beta}^{i}\phi_{\beta}\left(\tilde{\mu}_{\beta}^{i} - \tilde{\mu}_{\alpha}^{i}\right) - \sum_{\beta=1}^{N}\dot{\phi}_{\beta}\left(c_{\beta}^{i} - c_{\alpha}^{i}\right) \tag{6}$$

Eq. (5) is the diffusion equation in the interface region as in the conventional MPFM. Eq. (6) is called the interface partitioning rate equation in this study. Eq. (6) is implicitly solved to be convergent at each time step by the successive relaxation method. Moreover, in the quasi-equilibrium MPFM, partitioned solute element compositions were obtained by the parallel tangent law:

$$\tilde{\mu}_{\alpha}^{i}\left(c_{\alpha}^{i}\right) = \tilde{\mu}_{\beta}^{i}\left(c_{\beta}^{i}\right) \tag{7}$$

Eq. (7) was solved by the Newton–Rapson method. The different parts of the numerical program code for non- and quasi-equilibrium MPFMs solved Eqs. (6) and (7), respectively. Other parts were common in both MPFM codes. Therefore, microstructural evolution differences between non- and quasi-equilibrium MPFMs were obtained.

Anisotropic properties of dendritic or cellular growth were considered in Eq. (1). A two-dimensional model [28] was employed to define the interfacial energy and the interface mobility between liquid and solid phases using

$$\sigma_{\alpha\beta}\left(\theta\right) = \overline{\sigma}_{\alpha\beta}\left[1 + \varepsilon_{4}\cos\left(4\theta\right)\right] \tag{8}$$

$$K_{\alpha\beta}\left(\theta\right) = \overline{K}_{\alpha\beta}\left[1 + \varepsilon_{4}\cos\left(4\theta\right)\right] \tag{9}$$

doi:10.20944/preprints202103.0295.v1

respectively, where $\alpha = \mathrm{FCC}$ and $\beta = \mathrm{Liquid}$. θ is the angle of the normal vector on the interface and is given by $\theta = \tan^{-1}\{(\partial\emptyset_\alpha/\partial y)/(\partial\emptyset_\alpha/\partial x)\}$. ε_4 is the coefficient of four-fold symmetry, where 0.0167 and 0.25 were selected for the interfacial energy and the interface mobility, respectively. The anisotropy functions were not given for the interface between γ grains in the present calculations.

2.2. *Sublattice Model of γ in the CALPHAD framework*

The Ni(Bal.)–Al–Co–Cr–Mo–Ta–Ti–W–C alloy was selected to simulate the solidification microstructure of γ (FCC phase). The thermodynamics values, Gibbs free energy, and chemical potential of FCC and liquid phases were numerically provided from CALPHAD databases. In this study, the Ni database of Thermo-Calc, TCNI9 [29], was applied to obtain the thermodynamics values using Thermo-Calc TQ-Interface [30], which is a FORTRAN subroutine module. The numeric modules of TQ-Interface should be used for MPFM calculation to reduce the CPU time. Because this quick numeric module does not directly provide chemical potential values, the sublattice structure has to be considered in programming to estimate thermodynamic values.

The CALPHAD crystal structure of γ consisting of Ni(Bal.)–Al–Co–Cr–Mo–Ta–Ti–W–C was described by substitutional and interstitial sublattices, [Al, Co, Cr, Mo, Ni, Ta, Ti, W]m[C, Va]l, where m and l are units for the FCC phase and Va, which indicates the vacancy at the C site in the second sublattice. Chemical potentials for elements, μ_C , μ_j, j = Al, Co, Cr, Mo, Ni, Ta, Ti, and W in the FCC phase were described as

$$\begin{cases} \mu_\mathrm{C} = \dfrac{1}{l}\left(\dfrac{\partial G'}{\partial y_\mathrm{C}} - \dfrac{\partial G'}{\partial y_\mathrm{Va}}\right), \\ \mu_\mathrm{j} = \dfrac{1}{m}G' - \dfrac{1}{l}\dfrac{c_\mathrm{C}}{1-c_\mathrm{C}}\left(\dfrac{\partial G'}{\partial y_\mathrm{C}} - \dfrac{\partial G'}{\partial y_\mathrm{Va}}\right) - \dfrac{1}{1-c_\mathrm{C}}\sum_{\mathrm{i,i\neq C}} x_\mathrm{i}\left(\dfrac{\partial G'}{\partial y_\mathrm{i}} - \dfrac{\partial G'}{\partial y_\mathrm{j}}\right), \\ \qquad \mathrm{j} = \mathrm{Al, Co, Cr, Mo, Ni, Ta, Ti, W} \end{cases} \tag{10}$$

where y_c, y_i are the site fractions of the element in the sublattices, and G' is the Gibbs free energy for the total effective site number in the unit lattice. TQ-interface provide a differential of G' with site fraction, $\partial G'/\partial y_\mathrm{i}$, by reading parameter values from the CALPHAD sublattice model database. The derivation of Eq. (10) is explained in Appendix A. Eq. (10) can be promptly expanded to any kind or number of element systems and provides fast computation capability. This derivation procedure is promptly applied to more than two sublattice structures, *e.g.*, γ' (order–disorder FCC_L12 phase) as explained in Appendix A.

2.3. *Computational Methods and Common Conditions*

Eqs. (1) and (5) were solved using the two-dimensional finite difference method by forwarding in time and centering in space. Constant grid width, Δx, and time step, Δt, were applied. Δt was estimated by maximum stability limitation values according to diffusivity obtained by the diffusion equation and interface mobility and interfacial energy in the MPFM equation. The interface region width, δ, was five times the grid width in all calculations in this study. The interface region was defined as the FCC phase order ($\emptyset_\mathrm{FCC}$) value from 2.5×10^{-5} to $(1 - 2.5 \times 10^{-5})$. Bulk liquid and FCC phases were defined by $0 \leqq \emptyset_\mathrm{FCC} < 2.5 \times 10^{-5}$ and $(1 - 2.5 \times 10^{-5}) < \emptyset_\mathrm{FCC} \leqq 1$, respectively.

Initial Ni alloy composition was selected as Ni(Bal.)–3.2Al–0.1C–8.5Co–16.3Cr–1.65Mo–1.8Ta–3.22Ti–2.7W (wt.%) in this study. As-cast microstructure contained almost only γ (FCC phase) grains based on our experimental measurements. Initial solidified γ (FCC phase) appears at 1630.9 K by the equilibrium property calculation using Thermo-Calc software. Initial temperature values were set at 1621 K (undercooled state). The diffusivity of γ varied with temperature (Arrhenius equation) and was estimated using the diffusion database of Thermo-Calc [31]. The diffusivity of liquid, D_{L}, was set as 2.0×10^{-9} $\mathrm{m^2/s}$ for all calculations in this study.

2.4. Permeability Value

Zhang *et. al.* proposed the interface permeability equation related to the bulk diffusion mobilities as follows [25]:

$$P^{i}_{\text{FCC, Liquid}} = 8\frac{\phi_{\text{FCC}} V_m^{\text{FCC}} \tilde{M}_i^{\text{FCC}} + \phi_{\text{Liquid}} V_m^{\text{Liquid}} \tilde{M}_i^{\text{Liquid}}}{a\,\delta} \tag{11}$$

where $\tilde{M}_{\mathrm{i}}^{\mathrm{FCC}}$ and $\tilde{M}_{\mathrm{i}}^{\mathrm{Liquid}}$ are the diffusion mobilities of element i in bulk FCC and liquid phases, respectively, and $V_{\mathrm{m}}^{\mathrm{FCC}}$ and $V_{\mathrm{m}}^{\mathrm{Liquid}}$ are the molar volumes of FCC and liquid phases, respectively. a is the physical interface length at the atomistic scale. Eq. (11) shows an interpolating formulation by two terms, which vary with the phase order $\emptyset_{\mathrm{FCC}}$ where $\emptyset_{\mathrm{Liquid}} = 1 - \emptyset_{\mathrm{FCC}}$. The former (FCC) and the latter (liquid) were evaluated as follows: Diffusion mobility values were estimated using the diffusion mobility database MOBNI5 for the equilibrium compositions of the alloy Ni(Bal.)–3.2Al–0.1C–8.5Co–16.3Cr–1.65Mo–1.8Ta–3.22Ti–2.7W (wt.%) at 1626K. $\tilde{M}_{\mathrm{i}}^{\mathrm{FCC}}$ values were obtained as $1.72\times10^{-18}{\sim}4.02\times10^{-17}\ \mathrm{m^2{\cdot}mol/J/s}$ for the substitutional elements and $2.03\times10^{-14}\ \mathrm{m^2{\cdot}mol/J/s}$ for the interstitial element C. $\tilde{M}_{\mathrm{i}}^{\mathrm{Liquid}}$ values were obtained as $1.14{\sim}2.10\times10^{-13}\ \mathrm{m^2{\cdot}mol/J/s}$ for the substitutional elements and $6.91\times10^{-13}\ \mathrm{m^2{\cdot}mol/J/s}$ for the interstitial element C. The molar volumes $V_{\mathrm{m}}^{\mathrm{FCC}}$ and $V_{\mathrm{m}}^{\mathrm{Liquid}}$ were approximated as $8.0\times10^{-6}\ \mathrm{m^3/mol}$. The physical interface length was assumed as 2 nm. The former (FCC) term, $8\cdot V_{\mathrm{m}}^{\mathrm{FCC}}\tilde{M}_{\mathrm{i}}^{\mathrm{FCC}}/a/\delta$, led to $1.01\times10^{-6}{\sim}2.36\times10^{-5}\ \mathrm{m^3/J/s}$ for the substitutional elements and $1.19\times10^{-2}\ \mathrm{m^3/J/s}$ for the interstitial element C. The latter term (liquid), $8\cdot V_{\mathrm{m}}^{\mathrm{Liquid}}\tilde{M}_{\mathrm{i}}^{\mathrm{Liquid}}/a/\delta$, led to $7.30\times10^{-2}{\sim}0.13\times\ \mathrm{m^3/J/s}$ for the heavy elements and $0.44\ \mathrm{m^3/J/s}$ for the light element C. Further, the maximum number of the permeability $P^{i}_{\text{FCC, Liquid}}$ to maintain numerical stability was found as $\sim4\times10^{-5}\ \mathrm{m^3/J/s}$ by applying the same permeability value to all elements. This number had the same order as the former (FCC) term, $8\cdot V_{\mathrm{m}}^{\mathrm{FCC}}\tilde{M}_{\mathrm{i}}^{\mathrm{FCC}}/a/\delta$, for the substitutional elements and was smaller than that of the interstitial element C or the permeability defined by the liquid, $8\cdot V_{\mathrm{m}}^{\mathrm{Liquid}}\tilde{M}_{\mathrm{i}}^{\mathrm{Liquid}}/a/\delta$. If the solute element partition is controlled by reducing the diffusion mobility between the two phases, the permeability would be decided by the minimized value. The following solidification microstructure evolution was calculated based on a permeability value of $10^{-5}\ \mathrm{m^3/J/s}$ in this study.

3. Equiaxed Microstructure Evolution

3.1. Specific Model Conditions for Equiaxed Microstructure Evolution

The region was set as a square with 200 × 200 grid points. The grid width was 2.0×10^{-8} m. The initial γ grains, whose number was set as seven, were randomly distributed for nucleation. Their diameter was defined as one grid size. The grain crystalline directions were also randomly provided. The interfacial energy and the interface mobility between the liquid phase and γ were set to $0.2\ \mathrm{J/m^2}$ and $2.0\times10^{-8}\ \mathrm{m^4/J/s}$, respectively. The permeability $P^{i}_{\text{FCC, Liquid}}$ value was defined as $2\times10^{-5}\ \mathrm{m^3/J/s}$ for the non-equilibrium MPFM calculations. Uniform temperature (zero temperature gradient) was assumed. The calculations were performed in four cooling rates, 10^4 K/s, 10^5 K/s, 10^6 K/s, and 10^7 K/s. The initial temperature values were set at 1621 K to avoid initial γ grains from disappearing by the Gibbs–Thomson effect. Periodic boundary conditions were adapted for solving the MPFM and diffusion equations. The same conditions were supplied for the non- and quasi-equilibrium calculations.

3.2. Results and Discussion

Figures 1 and 2 show the solidification microstructure distributions at a cooling rate of 10^5 K/s by non- and quasi-equilibrium calculations, respectively, at 0.06 ms showing solute concentration and γ grain distributions. The solute diffusion and partitioning around the advancing interface between liquid and solid phases were precisely calculated for all elements. The segregation between grain interfaces was also confirmed. The random anisotropy between the liquid phase and γ grains was activated. We found that the solidification in the quasi-equilibrium MPFM (Figure 2) was more advanced than that in the non-equilibrium MPFM (Figure 1).

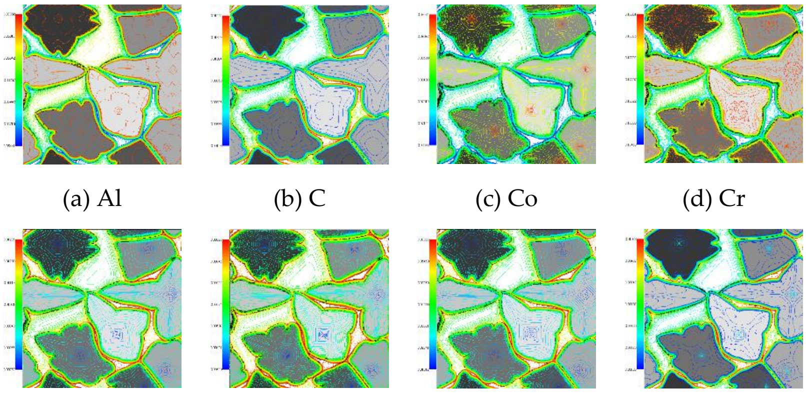

(a) Al (b) C (c) Co (d) Cr

(e) Mo (f) Ta (g) Ti (h) W

Figure 1. Solute concentration and γ grain distributions obtained by the non-equilibrium MPFM at 0.06 ms at a cooling rate of 10^5 K/s. **(a)**, **(b)**, **(c)**, **(d)**, **(e)**, **(f)**, **(g)**, and **(h)** are Al, C, Co, Cr, Mo, Ta, Ti, and W molar fractions, respectively.

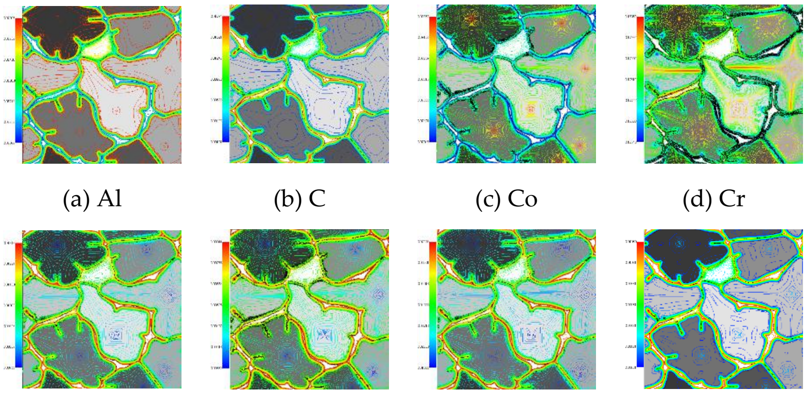

(a) Al (b) C (c) Co (d) Cr

(e) Mo (f) Ta (g) Ti (h) W

Figure 2. Solute concentration and γ grain distributions obtained by the quasi-equilibrium MPFM at 0.06 ms at a cooling rate of 10^5 K/s. **(a)**, **(b)**, **(c)**, **(d)**, **(e)**, **(f)**, **(g)**, and **(h)** are Al, C, Co, Cr, Mo, Ta, Ti, and W molar fractions, respectively.

The solidification microstructure evolutions were compared by changing the cooling rate for the two models. Figure 3 shows the temporary solidification microstructure distributions at a cooling rate of 10^4 K/s using non- and quasi-equilibrium MPFMs. The solute element C was selected to visualize solute concentration distribution. γ grain sizes obtained from the two MPFMs were similar. The solute distributions were also very close to each other. Figure 4 shows the temporary solidification microstructure distributions at a cooling rate of 10^7 K/s. The solidification obtained using the quasi-equilibrium MPFM advanced more compared with that using the non-equilibrium MPFM. Thus, the difference in the solidification rate between non- and quasi-equilibrium MPFMs increased as the cooling rate increased under the same conditions.

(a) Non-equilibrium MPFM

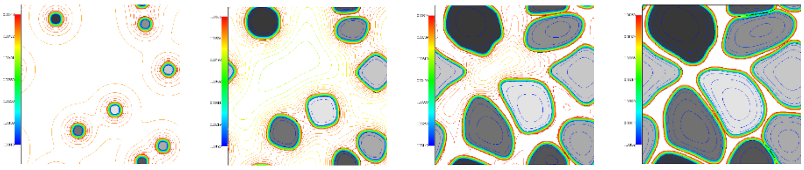

(1) 0.05ms (2) 0.15ms (3) 0.3ms (4) 0.6ms

(b) Quasi-equilibrium MPFM

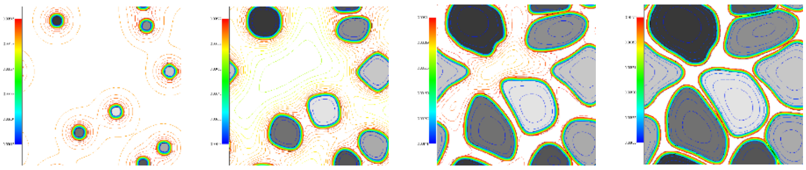

(1) 0.05ms (2) 0.15ms (3) 0.3ms (4) 0.6ms

Figure 3. Temporal C concentration (molar fraction) and γ grain distributions obtained at a cooling rate of 10^5 K/s by **(a)** the non-equilibrium MPFM and **(b)** the quasi-equilibrium MPFM.

(a) Non-equilibrium MPFM

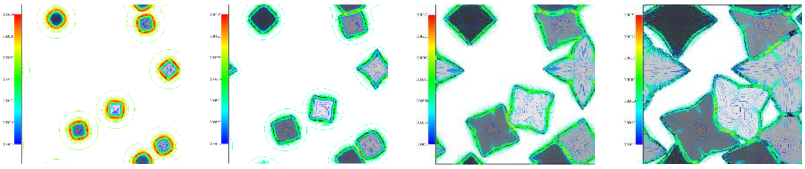

(1) 0.005ms (2) 0.008ms (3) 0.012ms (4) 0.015ms

(b) Quasi-equilibrium MPFM

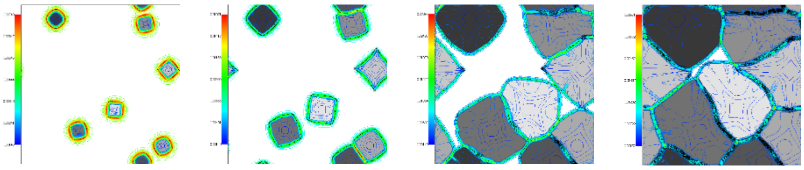

(1) 0.005ms (2) 0.008ms (3) 0.012ms (4) 0.015ms

Figure 4. Temporal C concentration (molar fraction) and γ grain distributions obtained at a cooling rate of 10^7 K/s by **(a)** the non-equilibrium MPFM and **(b)** the quasi-equilibrium MPFM.

Figure 5 shows the relations of temperature versus FCC phase (γ) area fraction for cooling rates of 10^4 K/s, 10^5 K/s, 10^6 K/s, and 10^7 K/s for non- and quasi-equilibrium MPFMs and the Scheil model (Thermo-Calc) calculation considered carbon back-diffusion. The difference between the temperature–FCC phase fraction profiles obtained from Scheil and MPFM calculations increased with the increased cooling rate. Under relatively low cooling rates, solidification interface motion is mainly controlled by the constitutional under cooling of the solute diffusion. If the cooling rate gradually decreases to zero, the solute concentration distribution around the interface nears that obtained by the Scheil model, which is assumed infinite under zero solute diffusivity for the liquid and solid, respectively, except for the infinite diffusivity of C in the solid. The results at 10^4 K/s are close to those obtained by the Scheil model, except for the initial undercooling period. Thermal undercooling will be the majority for solidification interface moving with increasing the cooling rate [32]. Thus, the growth rate under a higher cooling rate accelerates in the early stage and strongly decelerates as it nears the local equilibrium at the interface in the final stage.

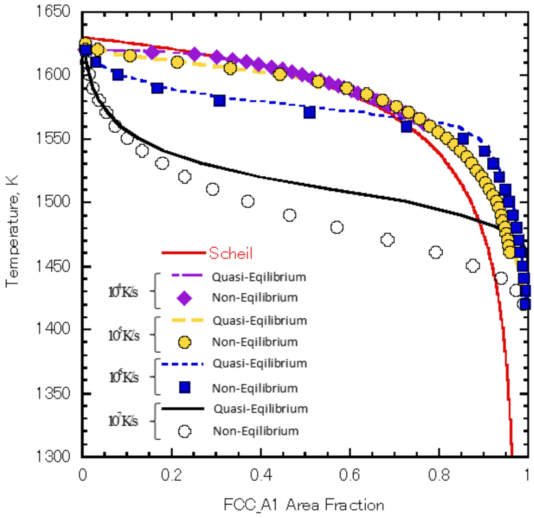

Figure 5. Temperature variations versus FCC area fraction at various cooling rates (10^4 K/s, 10^5 K/s, 10^6 K/s, and 10^7 K/s) for non- and quasi-equilibrium MPFMs and the Scheil model.

It can be seen that the temperature–FCC phase (γ) fraction profiles between non-equilibrium and quasi-equilibrium MPFMs almost coincide with each other at cooling rates lower than 10^5 K/s. Further, this difference gradually grows for cooling rates higher than 10^6 K/s at which the quasi-equilibrium MPFM growth rate is larger than the non-equilibrium MPFM growth rate. The non-equilibrium solidification is strengthened at above 10^6 K/s in the present alloy composition. It is well known that the non-equilibrium distribution (segregation) coefficient increases with the growth rate [33]. Karayagiz *et. al.* reported that the non-equilibrium distribution coefficient, k_v, increased with the growth rate due to the columnar microstructure evolution using the non-equilibrium MPFM for the Ni–Nb binary system [23]. They also found that k_v of the non-equilibrium MPFM calculation approached asymptotically to one of the quasi-equilibrium MPFM with the increase in permeability. As the permeability is a strength factor for segregation partitioning, it is expected that the temperature–FCC phase fraction profile obtained by the non-equilibrium MPFM will be close to that obtained by the quasi-equilibrium MPFM profile at increased permeability as the same tendency was confirmed for the γ–α transformation [34].

Figure 6 shows the temperature–FCC phase fraction profiles of the non-equilibrium and quasi-equilibrium MPFMs, varied with permeability values of 1×10^{-5} m^3/J/s, 2×10^{-5} m^3/J/s, and 4×10^{-5} m^3/J/s at a cooling rate of 10^7 K/s. It can be seen that the non-equilibrium profiles gradually get closer to the quasi-equilibrium ones. At a permeability of 4×10^{-5} m^3/J/s, profiles are almost the same for the two methods. It was confirmed that the permeability 4×10^{-5} m^3/J/s was the maximum value because calculations in the condition of the permeability over this value caused numerical instability. As it is explained in Section 2.3, the permeability value was determined in precision of digit order, so far. However, the evaluation of the non-equilibrium property for different cooling rates is available in the present non-equilibrium MPFM calculation procedure.

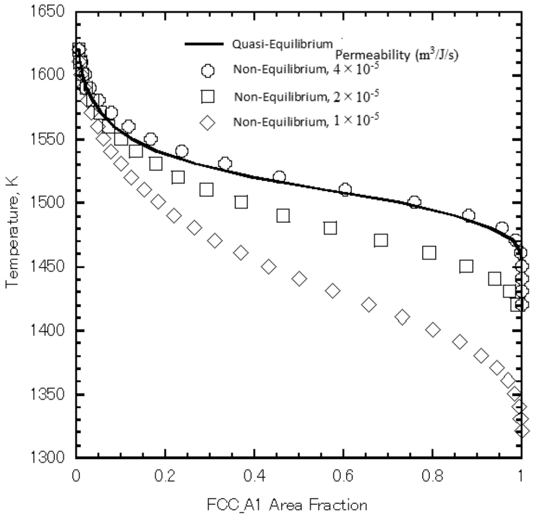

Figure 6. Temperature variation versus FCC area fraction at permeability values of 1×10^{-5} m^3/J/s, 2×10^{-5} m^3/J/s, and 4×10^{-5} m^3/J/s at a cooling rate of 10^7 K/s.

4. Columnar Microstructure Evolution

In the previous section, the permeability value, 4×10^{-5} m^3/J/s, was estimated to give the approximately equal equiaxed-solidification fraction rate for non- and quasi-equilibrium MPFM calculations at a cooling rate of 10^7 K/s. The microstructure evolution difference for the two methods will be confirmed in this section at a steady growth rate, $\bar{v} = 0.1\text{m/s}$, for various cooling rates and temperature gradients using the permeability value, 4×10^{-5} m^3/J/s.

4.1. Specific Model Conditions for Columnar Microstructure Evolution

The grid width was 1.0×10^{-8} m, which was defined to place four grids in the diffusion boundary layer length of the liquid side, $\delta_\mathrm{L} = 2D_\mathrm{L}/\bar{v} = 4 \times 10^{-8}$m. The cooling rate and the temperature gradient for the vertical direction were uniformly applied. The four combinations of the cooling rate and the temperature gradient were set, as shown in Table 1. The calculation region was set as a rectangle with 250 × 1500 grid points. However, 250 × 2000 grid points were applied to Case (a) to obtain steady growth. The initial γ grain was placed at the bottom as a film. The initial bottom temperature was set at 1621 K as for the previous equiaxed microstructure evolution condition. The time step was adapted as 1.0×10^{-8} s in all cases (Table 1). The symmetrical boundary conditions for the MPFM and diffusion equations were adapted for horizontal and vertical directions. The other conditions were the same as those defined in Sections 2.3. and 3.1.

Table 1. Variations in cooling rate and temperature gradient at a steady interface growth rate (0.1 m/s).

Case	Cooling rate, R (K/s)	Temperature gradient, G (K/m)
(a)	5×10^5	5×10^6
(b)	1×10^6	1×10^7
(c)	5×10^6	5×10^7
(d)	1×10^7	1×10^8

4.2. Results and Discussion

Figure 7 shows the snapshots of the microstructures obtained by the quasi-equilibrium MPFM calculations for conditions listed in Table 1. All cases reached steady cellular microstructures with boundaries parallel to the vertical direction, and the cell spaces were maintained. The average cell space decreased from cases (a) to (d) with the increased cooling rate and temperature gradient. Three growth stages were obtained: initial growth, accelerated growth with fine cellular segregation, and decelerated growth forming the steady cell microstructure. Figure 8 shows interface moving velocity values with time for all cases. Each curve contains two inflection points, which are the boundaries between the three growth stages. In the second stage, the fine cellular segregation growth is accompanied by hard competition, which makes the segregation lines fluctuate and disappear. In the second stage, the interface velocity continues to accelerate over the steady growth rate, 0.1m/s. After the maximum velocity is reached, in the third stage, a steady cellular microstructure is gradually constructed with the deceleration of the interface velocity. The second stage length is shortened from Cases (a) to (c). However, in Case (d), there is no obvious transformation from the second to third stages. The fine segregation microstructure promptly becomes a steady state, as evidenced by the shortly overshot velocity of Case (d) in Figure 8. It is considered that Case (d) is in transition from the cellular to planar interface growth.

The overshot velocity value from the steady velocity, 0.1 m/s, monotonically increases with the decreased cooling rate. In the second stage, the fine cellular segregation period, the length increases with the increased overshot velocity. These tendencies are likely induced by the mandatory quasi-equilibrium assumption at the interface. The solute partitioning estimated by the quasi-equilibrium leads to a large interface driving force. The interface velocity continues to accelerate over a steady velocity up to beginning of competitive fine cellular segregation. Moreover, the balance between the solute partitioning, cell spacing length, and solute undercooling starts to be formed according to the classical solidification theory based on the local equilibrium [33]. Then, the interface velocity decreases and reaches a steady state by constructing a regular cellular microstructure. A higher cooling rate can reach a steady undercooling temperature faster. Thus, the second stage period of a higher-cooling-rate case is shorter than that of the lower-cooling-rate case.

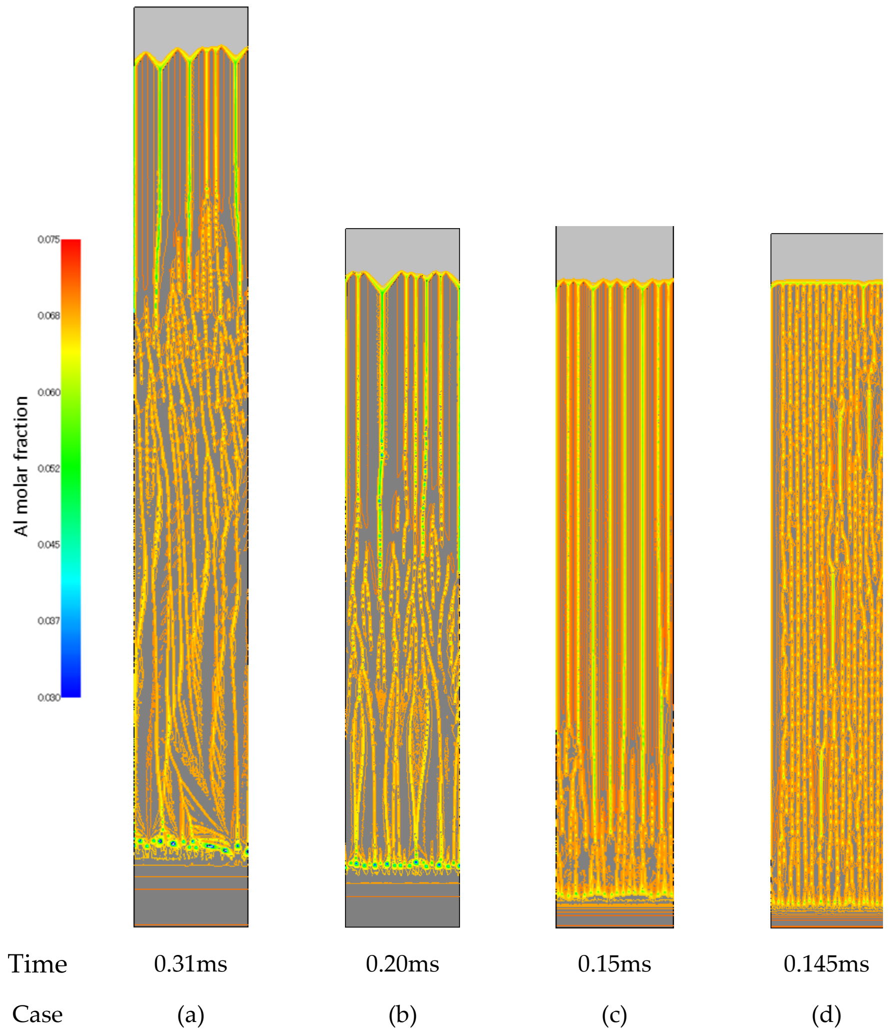

Figure 7. Snapshots of solidification microstructure distributions obtained by the quasi-equilibrium MPFM with Al concentration (molar fraction) at **(a)** 5×10^5 K/s and 5×10^6 K/m, **(b)** 1×10^6 K/s and 1×10^7 K/m, **(c)** 5×10^6 K/s and 5×10^7 K/m, and **(d)** 1×10^7 K/s and 1×10^8 K/m.

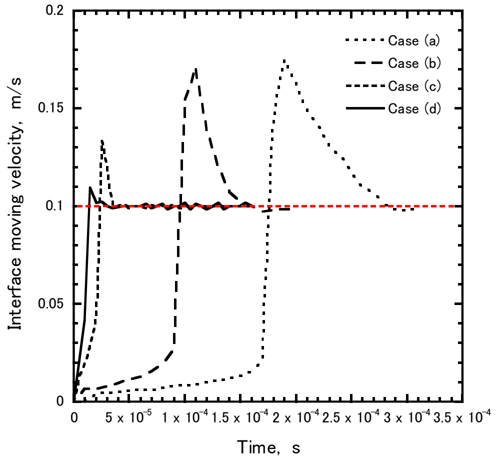

Figure 8. Interface moving velocity with time at **(a)** 5 × 10^5 K/s and 5 × 10^6 K/m, **(b)** 1 × 10^6 K/s and 1 × 10^7 K/m, **(c)** 5 × 10^6 K/s and 5 × 10^7 K/m, and **(d)** 1 × 10^7 K/s and 1 × 10^8 K/m, obtained by the quasi-equilibrium MPFM. The red dashed line indicates the steady velocity.

Figure 9 shows the snapshots of solidification microstructure distributions at Al concentration (molar fraction) obtained by the non-equilibrium MPFM under the conditions listed in Table 1. The interface moving velocity values with time are shown in Figure 10. The interface velocities of Cases (a) and (b) do not reach the steady value, 0.1 m/s. However, the steady cellular microstructures with constant cell spacing are formed at an early stage in all cases. The average cell space length decreases as the cooling rate and temperature gradient increase from cases (a) to (d). It is larger than that of the quasi-equilibrium MPFM case in all cases. The second stage of microstructure evolution constructed with competitive fine cellular segregation is not obvious in the non-equilibrium MPFM cases in Figure 9. The cellular microstructure promptly forms just after few cellular growth competitions followed by the initial planer interface broken in all cases. The overshooting tendency in Figure 10 is the opposite of those seen in Figure 8. Especially, in Cases (a) and (b), overshooting does not appear. In Cases (c) and (d), cell growth competitions are weak, regardless of the overshooting of the interface velocity. These results are considered to be led by the interface non-equilibrium assumption, which makes a lower driving force of constitutional undercooling due to more weakly solute portioning in the moving interface than the quasi-equilibrium assumption.

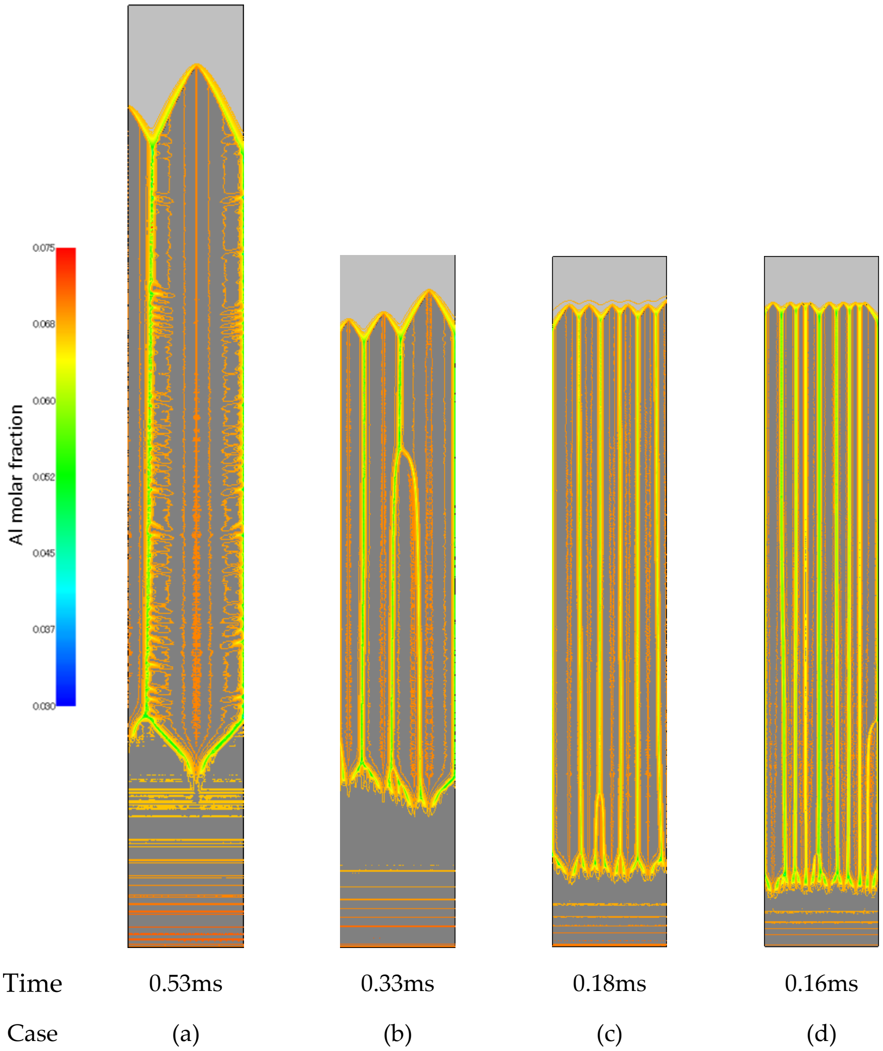

Figure 9. Snapshots of solidification microstructure distributions obtained by the non-equilibrium MPFM at Al concentration (molar fraction) at **(a)** 5 × 10^5 K/s and 5 × 10^6 K/m, **(b)** 1 × 10^6 K/s and 1 × 10^7 K/m, **(c)** 5 × 10^6 K/s and 5 × 10^7 K/m, and **(d)** 1 × 10^7 K/s and 1 × 10^8 K/m.

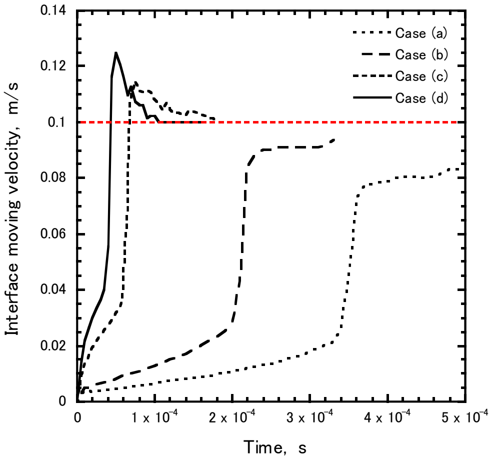

Figure 10. Interface moving velocity with time in Case (**a**): 5 × 10^5 K/s and 5 × 10^6 K/m, Case (**b**): 1 × 10^6 K/s and 1 × 10^7 K/m, Case (**c**): 5 × 10^6 K/s and 5 × 10^7 K/m, and Case (**d**): 1 × 10^7 K/s and 1 × 10^8 K/m obtained by the quasi-equilibrium MPFM. The red dashed line indicates the steady velocity.

The diffusional and thermal undercooling values are estimated, as shown in Figure 11. The liquidus temperatures, T_0 and T^*, for the initial alloy concentration and the cell tip concentration are obtained by Thermo-Calc, respectively. The undercooling temperature due to the curvature of the cell tip was not considered in this discussion because of the similarity of tip shapes in Figures 7 and 9. Figure 12 shows the diffusional and thermal undercooling values in the cell tips in Figures 7 and 9. The thermal undercooling values are much larger than diffusional undercooling ones. It is well known that the fraction of thermal undercooling increases with the increased cooling rate. It is reported that the fraction of thermal undercooling becomes approximately 80% at a cooling rate of 100 K/s and a temperature gradient of 1000 K/m for the Al–Cu alloy [32]. Figure 12 qualitatively agrees with this relation. The diffusional undercooling difference between non-equilibrium and quasi-equilibrium MPFMs is not much because liquid solute compositions at the tips have almost the same values, and liquidus temperature differences are less than five degrees, (Figures 7 and 9). Further, the thermal undercooling of the non-equilibrium MPFM is about from twice to three times larger than that of the quasi-equilibrium MPFM in each case. So, in the non-equilibrium MPFM, the solidification microstructure evolution is driven more by thermal undercooling than that in the quasi-equilibrium MPFM at a high cooling rate. The necessity of high thermal undercooling in the non-equilibrium MPFM arises from its weaker solute partitioning, which leads to weak constitutional undercooling. Then, the weak constitutional driving force is compensated by the thermal undercooling to achieve a steady interface velocity (0.1 m/s). In the previous equiaxed microstructure evolution, the permeability value is calibrated to adjust the solidification phase fraction varying with temperature between non- and quasi-equilibrium MPFMs. However, it is found that the difference in the columnar microstructure evolution between two MPFMs appears despite using the calibrated permeability.

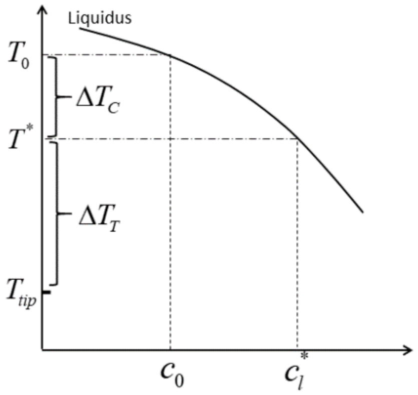

Figure 11. Schematic illustration of diffusional undercooling, ΔT_C, and thermal undercooling, ΔT_T, where c_0 is the initial alloy concentration, c_l^* and T_{tip} are the liquid concentration and temperature at the tip of the cell, respectively.

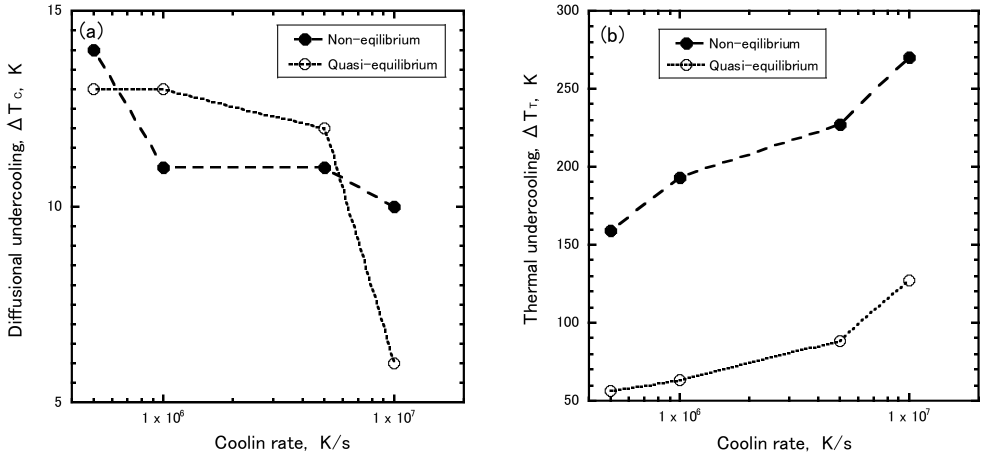

Figure 12. Undercooling with cooling rate: **(a)** diffusional undercooling; **(b)** thermal undercooling.

In Figure 9, number of cells at Case (a) of the non-equilibrium MPFM is few. It is considered to be more affected by horizontal boundary condition than other cases. An additional calculation using twice number of horizontal grid point, 500, was performed to reduce affection of the boundary condition. The snapshot of solidification microstructure distributions at Al concentration (molar fraction) is shown in Appendix B. Number of cells increased from 1.3 par 2.5μm in Figure 9 to 3.5 par 5μm in Appendix B. The average cell space changed from 1.92μm to 1.43μm. Following discussion uses the revised cell space, 1.43μm. Interface moving velocity and diffusional undercooling at cell tip were confirmed to be approximately same as the previous results in Figures 10 and 12, respectively.

Table 2 shows approximately average cell space values of Cases (a), (b), (c), and (d) for non- and quasi-equilibrium MPFMs. The ratios of the cell space in which the space of Case (a) is defined as a unit are shown in parenthesis. The ratios in the non-equilibrium MPFM decrease rapidly compared to those in the quasi-equilibrium MPFM. Karayagiz *et. al*. reported solidification microstructure simulation for Ni–3.2at.%Nb system by comparing with experimental measurements in various cooling rates and temperature gradients [23]. They estimated the ratio of the cell space as 0.35 for cooling rates from $5 \times 10^5 \mathrm{K/s}$ to $5 \times 10^6 \mathrm{K/s}$, which corresponds to Cases (a) to (c) in Table 2. It is quite close to the ratio, 0.32, obtained by the non-equilibrium MPFM. Further, the average cell space in the quasi-equilibrium MPFM is less decreasing as cooling rate from Cases (a) to (c).

Table 2. Average cell space (μm) at a steady interface moving velocity, 0.1 m/s. Numbers in parentheses are ratios of the cell space in which the space of Case (a) is defined as a unit.

Case	Non-equilibrium MPFM	Quasi-equilibrium MPFM
(a)	1.43 (1)	0.45 (1)
(b)	0.89 (0.62)	0.36 (0.8)
(c)	0.45 (0.32)	0.29 (0.64)
(d)	0.31 (0.22)	0.16 (0.35)

Figure 13 shows an as-cast microstructure obtained experimentally for the same alloy composition. The experiment was performed at a laser power of 300 W, beam scan velocity of 900 mm/s, beam spot diameter of 100 µm, and a powder layer depth of 30 µm, leading to a melt pool depth of about 100 µm. The cooling rate is estimated to be varying in the same range as in Table 1, from 10^5K/s to 10^6K/s digit orders, by thermal FEM analysis [36]. It can be seen that the morphology in Figure 13 is constructed by a cellular structure with a cell space around 1 µm. It is in good agreement with the non-equilibrium MPFM (Figure 9, Appendix B and Table 2). The quasi-equilibrium MPFM cell spaces in Figure 7 or Table 2 are too narrow compared to those in Figure 13. The fluctuated fine cellular segregation area, which is obtained by the quasi-equilibrium MPFM, is not identified in Figure 13. It is considered that the present non-equilibrium MPFM can accurately simulate rapid solidification in powder bed fusion processes.

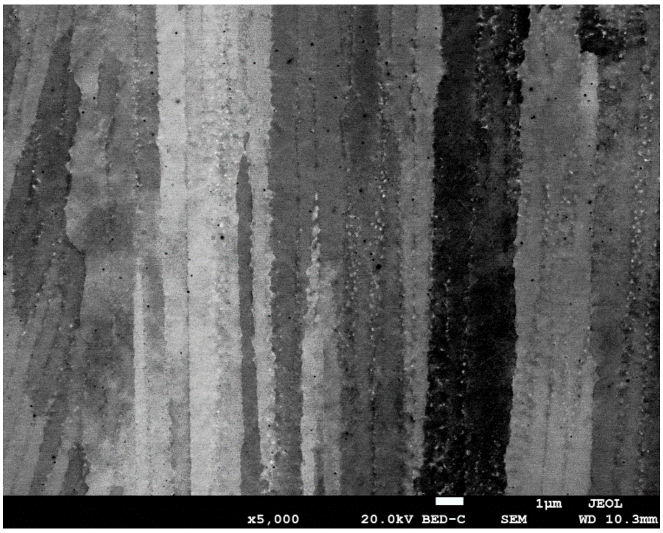

Figure 13. Solidified microstructure of Ni(Bal.)–3.2Al–0.1C–8.5Co–16.3Cr–1.65Mo–1.8Ta–3.22Ti–2.7W (wt.%) in the laser powder bed fusion process.

5. Conclusions

The non-equilibrium multi-phase field method using the finite interface dissipation model and the quasi-equilibrium multi-phase field method coupled with a CALPHAD database were employed for Ni(Bal.)–Al–Co–Cr–Mo–Ta–Ti–W–C. The equiaxed and columnar solidification microstructure evolutions of γ were performed in the LPBF thermal conditions by these methods. The main results and conclusion are summarized as follows:

1. The temperature–γ fraction relationships under a cooling rate of 10^5 K/s for non- and quasi-equilibrium MPFMs in the equiaxed simulations were in good agreement with each other. They were quite close to the Scheil model profile at 10^4 K/s.
2. The differences between non- and quasi-equilibrium methods grew with the cooling rate. The non-equilibrium solidification tendency was strengthened over the cooling rate 10^6 K/s.
3. Columnar solidification microstructure evolutions were performed in cooling rates from 5×10^5 K/s to 1×10^7 K/s at various temperature gradient values while maintaining a constant interface velocity, 0.1 m/s. The results showed that as the cooling rate increased,

the cell space decreased in both equilibrium methods. The average cell space in the non-equilibrium method was larger than that in the quasi-equilibrium method in each cooling rate.

4. The thermal undercooling of the non-equilibrium method was much larger than that of the quasi-equilibrium method, whereas the diffusional undercooling was almost the same for both.

5. The cell space of the non-equilibrium method agrees with experimental measurements better than that of the quasi-equilibrium method. The non-equilibrium MPFM gives us a more accurate solidification microstructure estimation tool in LPBF.

Author Contributions: Conceptualization, S.N.; methodology, S.N. and M.S.; software, S.N.; validation, S.N. and W.M.; funding acquisition, W.M.; supervision, W.M. All authors have read and agreed to the published version of the manuscript.

Funding: This work was partially supported by JST under Cross-ministerial Strategic Innovation Promotion Program (SIP). In addition, part of this research was supported by Strategic Innovation Program for Energy Conservation Technologies (New Energy and Industrial Technology Development Organization: NEDO)

Acknowledgments: Partially financial support from Cross-ministerial Strategic Innovation Promotion Program (SIP), "Materials Integration' for revolutionary design system of structural materials" (Funding agency: JST) is gratefully acknowledged. Partially financial support from Strategic Innovation Program for Energy Conservation Technologies, NEDO, is also gratefully acknowledged.

Conflicts of Interest: The authors declare no conflict of interest.

Appendix A

General representation of the chemical potential for the FCC_L12 phase using the CALPHAD sublattice model constructed by substitutional and interstitial elements

The CALPHAD model of FCC_L12 phase for Ni(Bal.)–Al–Co–Cr–Mo–Ta–Ti–W–C is explained by the order–disorder sublattice model, which is constructed by two sublattices for the substitutional elements and a sublattice for the interstitial element C, as shown by (Al#1, Co#1, Cr#1, Mo#1, Ni#1, Ta#1, Ti#1, W#1)m (Al#2, Co#2, Cr#2, Mo#2, Ni#2, Ta#2, Ti#2, W#2)n (C, Va)l, where m, n, and l are the site numbers of the first, second, and third sublattices, respectively. The chemical potential of each element is given by

$$\begin{cases} \mu_{\mathrm{Ni}} = G - \left.\dfrac{\partial G}{\partial c_{\mathrm{Al}}}\right|_{c_{\mathrm{Al}},c_{\mathrm{Ni}}} c_{\mathrm{Al}} - \left.\dfrac{\partial G}{\partial c_{\mathrm{Co}}}\right|_{c_{\mathrm{Co}},c_{\mathrm{Ni}}} c_{\mathrm{Co}} - \left.\dfrac{\partial G}{\partial c_{\mathrm{Cr}}}\right|_{c_{\mathrm{Cr}},c_{\mathrm{Ni}}} c_{\mathrm{Cr}} - \left.\dfrac{\partial G}{\partial c_{\mathrm{Mo}}}\right|_{c_{\mathrm{Mo}},c_{\mathrm{Ni}}} c_{\mathrm{Mo}} \\ \qquad - \left.\dfrac{\partial G}{\partial c_{\mathrm{Ta}}}\right|_{c_{\mathrm{Ta}},c_{\mathrm{Ni}}} c_{\mathrm{Ta}} - \left.\dfrac{\partial G}{\partial c_{\mathrm{Ti}}}\right|_{c_{\mathrm{Ti}},c_{\mathrm{Ni}}} c_{\mathrm{Ti}} - \left.\dfrac{\partial G}{\partial c_{\mathrm{W}}}\right|_{c_{\mathrm{W}},c_{\mathrm{Ni}}} c_{\mathrm{W}} - \left.\dfrac{\partial G}{\partial c_{\mathrm{C}}}\right|_{c_{\mathrm{C}},c_{\mathrm{Ni}}} c_{\mathrm{C}} \\ \quad = G - \left.\dfrac{\partial G}{\partial x_{\mathrm{C}}}\right|_{c_{\mathrm{C}},c_{\mathrm{Ni}}} c_{\mathrm{C}} - \sum_{\mathrm{i,i\neq Ni,C}} \left.\dfrac{\partial G}{\partial c_{\mathrm{i}}}\right|_{c_{\mathrm{i}},c_{\mathrm{Ni}}} c_{\mathrm{i}}, \\ \mu_{\mathrm{i}} = \mu_{\mathrm{Ni}} + \left.\dfrac{\partial G}{\partial c_{\mathrm{i}}}\right|_{\mathrm{Ni,i}}, \qquad \text{where} \quad \text{i=Al, Co, Cr, Mo, Ta, Ti, W, C} \end{cases} \tag{A-1}$$

where $|_{\mathrm{Ni,\,i}}$ indicates the differential operation on the coordinate between the solvent Ni and the solute element i. The quick subroutine of Thermo-calc TQ-Interface gives a differential value only by the site fraction for each sublattice. Site fraction is defined by the fraction of an element occupying the site of a sublattice. The molar-differential terms in Eq. (A-1) have to be converted to the formulations using site fractions.

The Gibbs free energy for the total site number of the unit lattice, G', is given by the TQ-Interface subroutine. So, the Gibbs free energy per unit mole, G, is given by

$$G=\frac{1}{m+n+ly_{\mathrm{C}}}G'=\frac{1-c_{\mathrm{C}}}{m+n}G' \tag{A-2}$$

where the relation $1/(m+n+ly_{\mathrm{c}})=(1-c_{\mathrm{C}})/(m+n)$ is adapted. y_{C} is the site fraction of C in the third sublattice. The molar-differential terms in Eq. (A-1) can be changed to the following equations using Eq. (A-2) and the chain rule of differentiation,

$$\left.\frac{\partial G}{\partial c_{\mathrm{C}}}\right|_{c_{\mathrm{C}},c_{\mathrm{Ni}}}=\frac{1}{m+n}\left.\frac{\partial(1-c_{\mathrm{C}})}{\partial c_{\mathrm{C}}}\right|_{c_{\mathrm{C}},c_{\mathrm{Ni}}}\cdot G'+\frac{1-c_{\mathrm{C}}}{m+n}\left[\begin{array}{l}\left.\frac{\partial G'}{\partial y_{\mathrm{C}}}\frac{\partial y_{\mathrm{C}}}{\partial c_{\mathrm{C}}}\right|_{c_{\mathrm{C}},c_{\mathrm{Ni}}}+\left.\frac{\partial G'}{\partial y_{\mathrm{Va}}}\frac{\partial y_{\mathrm{Va}}}{\partial c_{\mathrm{C}}}\right|_{c_{\mathrm{C}},c_{\mathrm{Ni}}}\\+\sum_{\mathrm{i,i\neq C}}\left.\frac{\partial G'}{\partial y_{\mathrm{i\#1}}}\frac{\partial y_{\mathrm{i\#1}}}{\partial y_{\mathrm{i}}}\frac{\partial y_{\mathrm{i}}}{\partial c_{\mathrm{C}}}\right|_{c_{\mathrm{C}},c_{\mathrm{Ni}}}+\sum_{\mathrm{i,i\neq C}}\left.\frac{\partial G'}{\partial y_{\mathrm{i\#2}}}\frac{\partial y_{\mathrm{i\#1}}}{\partial y_{\mathrm{i}}}\frac{\partial y_{\mathrm{i}}}{\partial c_{\mathrm{C}}}\right|_{c_{\mathrm{C}},c_{\mathrm{Ni}}}\end{array}\right],$$

$$\left.\frac{\partial G}{\partial c_{\mathrm{i}}}\right|_{c_{\mathrm{i}},c_{\mathrm{Ni}}}=\frac{1}{m+n}\left.\frac{\partial(1-c_{\mathrm{C}})}{\partial c_{\mathrm{i}}}\right|_{c_{\mathrm{i}},c_{\mathrm{Ni}}}\cdot G'+\frac{1-c_{\mathrm{C}}}{m+n}\left[\begin{array}{l}\left.\frac{\partial G'}{\partial y_{\mathrm{C}}}\frac{\partial y_{\mathrm{C}}}{\partial c_{\mathrm{i\#1}}}\frac{\partial c_{\mathrm{i\#1}}}{\partial c_{\mathrm{i}}}\right|_{c_{\mathrm{i}},c_{\mathrm{Ni}}}+\left.\frac{\partial G'}{\partial y_{\mathrm{C}}}\frac{\partial y_{\mathrm{C}}}{\partial c_{\mathrm{i\#2}}}\frac{\partial c_{\mathrm{i\#2}}}{\partial c_{\mathrm{i}}}\right|_{c_{\mathrm{i}},c_{\mathrm{Ni}}}\\+\left.\frac{\partial G'}{\partial y_{\mathrm{Va}}}\frac{\partial y_{\mathrm{Va}}}{\partial c_{\mathrm{i\#1}}}\frac{\partial c_{\mathrm{i\#1}}}{\partial c_{\mathrm{i}}}\right|_{c_{\mathrm{i}},c_{\mathrm{Ni}}}+\left.\frac{\partial G'}{\partial y_{\mathrm{Va}}}\frac{\partial y_{\mathrm{Va}}}{\partial c_{\mathrm{i\#2}}}\frac{\partial c_{\mathrm{i\#2}}}{\partial c_{\mathrm{i}}}\right|_{c_{\mathrm{i}},c_{\mathrm{Ni}}}\\+\sum_{\mathrm{j,j\neq C}}\left.\frac{\partial G'}{\partial y_{\mathrm{j\#1}}}\frac{\partial y_{\mathrm{j\#1}}}{\partial y_{\mathrm{i}}}\frac{\partial y_{\mathrm{i}}}{\partial c_{\mathrm{i}}}\right|_{c_{\mathrm{i}},c_{\mathrm{Ni}}}+\sum_{\mathrm{j,j\neq C}}\left.\frac{\partial G'}{\partial y_{\mathrm{i\#2}}}\frac{\partial y_{\mathrm{j\#2}}}{\partial y_{\mathrm{i}}}\frac{\partial y_{\mathrm{i}}}{\partial c_{\mathrm{i}}}\right|_{c_{\mathrm{i}},c_{\mathrm{Ni}}}\end{array}\right], \tag{A-3}$$

$$\text{i=Al, Co, Cr, Mo, Ta, Ti, W, C}$$

The relations between molar and site fractions of elements can be described as

$$\begin{cases}c_{\mathrm{C}}=\dfrac{ly_{\mathrm{C}}}{m+n+ly_{\mathrm{C}}},\\ c_{\mathrm{i\#1}}=\dfrac{m}{m+n}(1-c_{\mathrm{C}})y_{\mathrm{i\#1}},\\ c_{\mathrm{i\#2}}=\dfrac{n}{m+n}(1-c_{\mathrm{C}})y_{\mathrm{i\#2}},\\ c_{\mathrm{i}}=c_{\mathrm{i\#1}}+c_{\mathrm{i\#2}}=\dfrac{1-c_{\mathrm{C}}}{m+n}(my_{\mathrm{i\#1}}+ny_{\mathrm{i\#2}})=\dfrac{1-c_{\mathrm{C}}}{m+n}y_{\mathrm{i}}\end{cases} \tag{A-4}$$

where $y_{\mathrm{i\#1}}$ and $y_{\mathrm{i\#2}}$ are the site fractions of the substitutional elements in the first and second sublattices, respectively, and $y_{\mathrm{i}}\coloneqq my_{\mathrm{i\#1}}+ny_{\mathrm{i\#2}}$. The differential of the site fraction by a molar fraction is formulated with careful treatment for the coordinate between the solvent and selected solute composition using Eq. (A-4), as follows:

$$\begin{cases}\left.\dfrac{\partial y_{\mathrm{C}}}{\partial c_{\mathrm{C}}}\right|_{c_{\mathrm{C}},c_{\mathrm{Ni}}}=\dfrac{m+n}{l}\dfrac{\partial}{\partial c_{\mathrm{C}}}\left.\dfrac{c_{\mathrm{C}}}{1-c_{\mathrm{C}}}\right|_{x_{\mathrm{C}},x_{\mathrm{Ni}}}=\dfrac{m+n}{l}\dfrac{1}{(1-c_{\mathrm{C}})^2},\\ \left.\dfrac{\partial y_{\mathrm{V}}}{\partial c_{\mathrm{C}}}\right|_{c_{\mathrm{C}},c_{\mathrm{Ni}}}=\dfrac{\partial}{\partial c_{\mathrm{C}}}(1-y_{\mathrm{C}})\Big|_{c_{\mathrm{C}},c_{\mathrm{Ni}}}=-\dfrac{m+n}{l}\dfrac{1}{(1-c_{\mathrm{C}})^2},\\ \left.\dfrac{\partial y_{\mathrm{i}}}{\partial c_{\mathrm{C}}}\right|_{x_{\mathrm{C}},x_{\mathrm{Ni}}}=(m+n)\dfrac{\partial}{\partial c_{\mathrm{C}}}\left.\left(\dfrac{c_{\mathrm{i}}}{1-c_{\mathrm{C}}}\right)\right|_{c_{\mathrm{C}},c_{\mathrm{Ni}}}=\begin{cases}(m+n)\dfrac{1-c_{\mathrm{C}}-c_{\mathrm{i}}}{(1-c_{\mathrm{C}})^2}, & \text{i=Ni},\\ (m+n)\dfrac{c_{\mathrm{i}}}{(1-c_{\mathrm{C}})^2}, & \text{i} \neq \text{Ni}\end{cases},\\ \qquad\qquad\text{i = Al, Co, Cr, Mo, Ni, Ta, Ti, W}\end{cases} \tag{A-5}$$

$$\begin{cases} \left.\dfrac{\partial y_{\mathrm{C}}}{\partial c_{\mathrm{i\#1}}}\right|_{x_{\mathrm{i}},x_{\mathrm{Ni}}} = \dfrac{m+n}{l}\dfrac{\partial}{\partial c_{\mathrm{i\#1}}}\left.\dfrac{c_{\mathrm{C}}}{1-c_{\mathrm{C}}}\right|_{x_{\mathrm{i}},x_{\mathrm{Ni}}} = 0, \\ \left.\dfrac{\partial y_{\mathrm{V}}}{\partial c_{\mathrm{i\#1}}}\right|_{x_{\mathrm{i}},x_{\mathrm{Ni}}} = 0, \\ \left.\dfrac{\partial y_{\mathrm{C}}}{\partial c_{\mathrm{i\#2}}}\right|_{x_{\mathrm{C}},x_{\mathrm{Ni}}} = \dfrac{m+n}{l}\dfrac{\partial}{\partial c_{\mathrm{i\#2}}}\left.\dfrac{c_{\mathrm{C}}}{1-c_{\mathrm{C}}}\right|_{x_{\mathrm{C}},x_{\mathrm{Ni}}} = 0, \\ \left.\dfrac{\partial y_{\mathrm{V}}}{\partial c_{\mathrm{i\#2}}}\right|_{x_{\mathrm{C}},x_{\mathrm{Ni}}} = 0, \\ \qquad \mathrm{i} = \mathrm{Al, Co, Cr, Mo, Ta, Ti, W} \end{cases} \tag{A-6}$$

$$\begin{cases} \left.\dfrac{\partial y_{\mathrm{j}}}{\partial c_{\mathrm{i}}}\right|_{x_{\mathrm{i}},x_{\mathrm{Ni}}} = (m+n)\dfrac{\partial}{\partial c_{\mathrm{i}}}\left.\left(\dfrac{c_{\mathrm{j}}}{1-c_{\mathrm{C}}}\right)\right|_{x_{\mathrm{i}},x_{\mathrm{Ni}}} = \begin{cases} -(m+n)\dfrac{1}{1-c_{\mathrm{C}}}, & \mathrm{j{=}Ni} \\ (m+n)\dfrac{1}{1-c_{\mathrm{C}}}, & \mathrm{j{=}i} \\ 0, \quad \mathrm{j} \neq \mathrm{i} \end{cases}, \\ \mathrm{i} = \mathrm{Al, Co, Cr, Mo, Ta, Ti, W} \quad \mathrm{j} = \mathrm{Al, Co, Cr, Mo, Ni, Ta, Ti, W} \end{cases} \tag{A-7}$$

Substituting Eqs. (A-5), (A-6), and (A-7) into Eq. (A-3) leads to

$$\begin{cases} \mu_{\mathrm{C}} = \dfrac{1}{l}\left(\dfrac{\partial G'}{\partial y_{\mathrm{C}}} - \dfrac{\partial G'}{\partial y_{\mathrm{Va}}}\right), \\ \mu_{\mathrm{J}} = \dfrac{1}{m+n}G' - \dfrac{1}{l}\dfrac{c_{\mathrm{C}}}{1-c_{\mathrm{C}}}\left(\dfrac{\partial G'}{\partial y_{\mathrm{C}}} - \dfrac{\partial G'}{\partial y_{\mathrm{Va}}}\right) \\ \qquad - \dfrac{1}{1-c_{\mathrm{C}}}\sum_{\mathrm{i,i\neq C}} c_{\mathrm{i}}\left(\dfrac{\partial G'}{\partial y_{\mathrm{i\#1}}} - \dfrac{\partial G'}{\partial y_{\mathrm{J\#1}}}\right) - \dfrac{1}{1-x_{\mathrm{C}}}\sum_{\mathrm{i,i\neq C}} c_{\mathrm{i}}\left(\dfrac{\partial G'}{\partial y_{\mathrm{i\#2}}} - \dfrac{\partial G'}{\partial y_{\mathrm{J\#2}}}\right), \\ \qquad \mathrm{J} = \mathrm{Al, Co, Cr, Mo, Ni, Ta, Ti, W} \end{cases} \tag{A-8}$$

Furthermore, substituting Eq. (A-8) into Eq. (A-1) gives chemical potential equations:

$$\begin{cases} \mu_{\mathrm{C}} = \dfrac{1}{l}\left(\dfrac{\partial G'}{\partial y_{\mathrm{C}}} - \dfrac{\partial G'}{\partial y_{\mathrm{Va}}}\right), \\ \mu_{\mathrm{J}} = \dfrac{1}{m+n}G' - \dfrac{1}{l}\dfrac{c_{\mathrm{C}}}{1-c_{\mathrm{C}}}\left(\dfrac{\partial G'}{\partial y_{\mathrm{C}}} - \dfrac{\partial G'}{\partial y_{\mathrm{Va}}}\right) \\ \qquad - \dfrac{1}{1-c_{\mathrm{C}}}\sum_{\mathrm{i,i\neq C}} c_{\mathrm{i}}\left(\dfrac{\partial G'}{\partial y_{\mathrm{i\#1}}} - \dfrac{\partial G'}{\partial y_{\mathrm{J\#1}}}\right) - \dfrac{1}{1-c_{\mathrm{C}}}\sum_{\mathrm{i,i\neq C}} c_{\mathrm{i}}\left(\dfrac{\partial G'}{\partial y_{\mathrm{i\#2}}} - \dfrac{\partial G'}{\partial y_{\mathrm{J\#2}}}\right), \\ \qquad \mathrm{J} = \mathrm{Al, Co, Cr, Mo, Ni, Ta, Ti, W} \end{cases} \tag{A-9}$$

where G' and $\partial G'/\partial y_{\mathrm{i}}$,(i=C, Va, i#1, i#2) values are supplied as the output of TQ-Interface inputted by temperature and composition values. It can be understood that Eq. (A-9) has very systematic formations. So, it offers simple programming and fast computation. Therefore, it can be inductively extended for not only any number of elements and/or sublattices but also any solid solution sublattice models, such as BCC, HCP *et. al*. Eq. (10) for FCC_A1 phase is immediately derived by omitting the second sublattice term in Eq. (A-9).

Appendix B

Additional calculation using twice width, 5μm, for non-equilibrium MPFM in condition of Case (a), cooling rate 5 × 10⁵ K/s and temperature gradient 5 × 10⁶ K/m.

Calculation conditions were the same as the non-equilibrium MPFM for columnar microstructure evolution except for number of the horizontal grid points changed from 250 to 500. Figure B.1 shows the snapshot of solidification microstructure distribution at Al concentration (molar fraction).

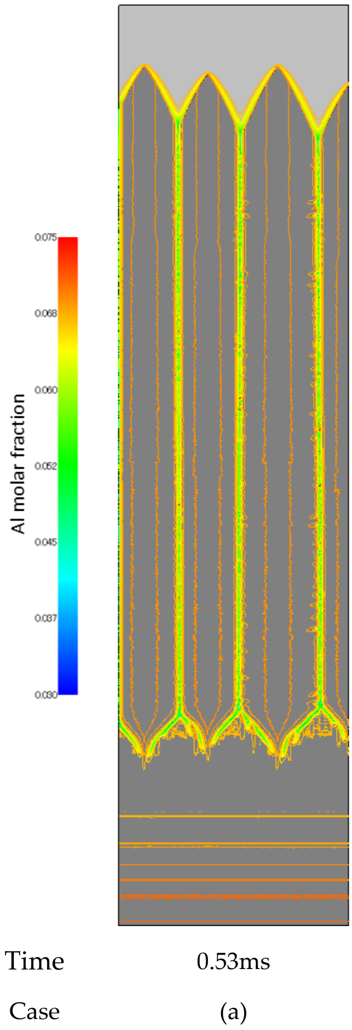

Figure B.1. Snapshot of solidification microstructure distributions obtained by the non-equilibrium MPFM at Al concentration (molar fraction) at **(a)** 5 × 10^5 K/s and 5 × 10^6 K/m by twice number of horizontal grid point, 500.

References

1. Gorsse, S.; Hutchinson, C.; Gouné, M.; Banerjee, R. Additive manufacturing of metals: A brief review of the characteristic microstructures and properties of steels, Ti-6Al-4V and high-entropy alloys. Science and Technology of Advanced Materials 2017, 18, 584-610.
2. Yan, F.; Xiong, W.; Faierson, E.. J. Grain structure control of additively manufactured metallic materials. Materials 2017, 10, 1260. doi.org/10.3390/ma10111260
3. Collins, P. C.; Brice, D. A.; Samimi, P.; Ghamarian, I.; Fraser, H. L. Microstructural control of additively manufactured metallic materials. Annual Review of Materials Research 2016, 46, 63-91
4. Kok, Y.; Tan, X. P.; Wang, P.; Nai, M. L. S.; Loh, N. H.; Liu, E.; Tor, S. B. Anisotropy and heterogeneity of microstructure and mechanical properties in metal additive manufacturing: A critical review. Materials and Design 2018, 139, 565-586. doi.org/10.1016/j.matdes.2017.11.021

5. Thampy, V.; Fong, A. F.; Calta, N. P.; Wang, J.; Martin, A. A.; depend P.J.; Kiss, A.M.; Guss, G.; Xing, Q.; Ott, R. T.; Buuren, A. V.; Toney, M. F. ; Weker, J. N.; Kramer, M. J.; Matthews, M. J.; Tassone, C. J.; Stone, K. H. Subsurface cooling rates and microstructural response during laser based metal additive manufacturing. Scientific Reports 2020 doi.org/10.1038/s41598-020-58598-z
6. Farshidianfar, M. H.; Khajepour, A.; Gerlich, A. P. Effect of real-time cooling rate on microstructure in Laser Additive Manufacturing. Journal of Materials Processing Technology 2016, 231, 468-478. doi.org/10.1016/j.jmatprotec.2016.01.017
7. Scipioni Bertoli, U. S.; Guss, G.; Wu, S.; Matthews, M. J.; Schoenung, J. M. In-situ characterization of laser-powder interaction and cooling rates through high-speed imaging of powder bed fusion additive manufacturing. Materials and Design 2017, 135, 385-396. doi.org/10.1016/j.matdes.2017.09.044
8. Promoppatum, P.; Yao, S.-C.; Pistorius, P. C.; Rollett, A. D.; Coutts, P. J.; Lia, F.; Martukanitz, R. Numerical modeling and experimental validation of thermal history and microstructure for additive manufacturing of an Inconel 718 product. Progress in Additive Manufacturing 2018, 3, 15-32. doi.org/10.1007/s40964-018-0039-1
9. Promoppatum, P.; Yao, S.-C.; Pistorius, P. C.; Rollett, A. D.; Coutts, P. J.; Lia, F.; Martukanitz, R. Numerical modeling and experimental validation of thermal history and microstructure for additive manufacturing of an Inconel 718 product. Progress in Additive Manufacturing 2018, 3, 15-32. doi.org/10.1007/s40964-018-0039-1
10. Karayagiz, K.; Elwany, A.; Tapia, G.; Franco, B.; Johnson, L.; Ma, J.; Karaman, I.; Arróyave, R. Numerical and experimental analysis of heat distribution in the laser powder bed fusion of Ti-6Al-4V IISE. Transactions 2019, 51, 136-152. doi.org/10.1080/24725854.2018.1461964
11. Watari, N.; Ogura, Y.; Yamazaki, N.; Inoue, Y.; Kamitani, K.; Fujiya, Y.; Toyoda, M.; Goya, S.; Watanabe, T. Two-fluid model to simulate metal powder bed fusion additive manufacturing. Journal of Fluid Science and Technology, 2018 13 No.17-00715 JFST0010-JFST0010. doi.org/10.1299/jfst.2018jfst0010
12. Song, J.; Chew, Y.; Bi, G.; Yao, X.; Zhang, B.; Bai, J.; Moon, S. K. Numerical and experimental study of laser aided additive manufacturing for melt-pool profile and grain orientation analysis. Materials and Design, 2018 137, 286-297. doi.org/10.1016/j.matdes.2017.10.033
13. Rolchigo, M. R.; Mendoza, M. Y.; Samimi, P.; Brice, D. A.; Martin, B.; Collins, P. C.; LeSar, R. Modeling of ti-W solidification microstructures under additive manufacturing conditions. Metallurgical and Materials Transactions A 2017, 48, 3606-3622
14. Lian, Y.; Gan, Z.; Yu, C.; Kats, D.; Liu, W. K.; Wagner, G. J. A cellular automaton finite volume method for microstructure evolution during additive manufacturing. Materials and Design 2019, 169. doi.org/10.1016/j.matdes.2019.107672
15. Ghosh, S.; McReynolds, K.; Guyer, J. E.; Banerjee, D. Simulation of temperature, stress and microstructure fields during laser deposition of Ti–6Al–4V. Modelling and Simulation in Materials Science and Engineering 2018, 26, 075005 (16pp)
16. Wang, X.; Liu, P. W.; Ji, Y.; Horstemeyer, M. H.; Chen, L.; D. Investigation on microsegregation of IN718 alloy during additive manufacturing via integrated phase-field and finite-element modeling. Journal of Materials Engineering and Performance 2018. doi.org/10.1007/s11665-018-3620-3
17. Yang, Y.; Kühn, P.; Yi, M.; Egger, H.; Xu, B.-X. Non-isothermal phase-field modeling of heat–melt–microstructure-coupled processes during powder bed fusion JOM 2020 72 1719-1733. doi.org/10.1007/s11837-019-03982-y
18. Acharya, R.; Sharon, J. A.; Staroselsky, A. Prediction of microstructure in laser powder bed fusion process. Acta Materialia 2017, 124, 360-371. doi.org/10.1016/j.actamat.2016.11.018
19. Wu, L.; Zhang, J., Phase field simulation of dendritic solidification of Ti-6Al-4V during additive manufacturing process *JOM* 2018 doi.org/10.1007/s11837-018-3057-z
20. Boussinot, G.; Apel, M.; Zielinski, J.; Hecht, U.; Schleifenbaum, J. H. Strongly out-of-equilibrium columnar solidification during the Laser Powder-Bed Fusion additive manufacturing process. Physical Review Applied 2019, 11, 014025
21. Steinbach, I.; Zhang, L.; Plapp, M. Phase-field model with finite interface dissipation. Acta Materialia 2012, 60, 2689-2701. doi.org/10.1016/j.actamat.2012.01.035
22. Zhang, L.; Steinbach, I. Phase-field model with finite interface dissipation: Extension to multi-component multi-phase alloys. Acta Materialia 2012, 60, 2702-2710. doi.org/10.1016/j.actamat.2012.02.032
23. Karayagiz, K.; Johnson, L.; Seede, R.; Attari, V.; Zhang, B.; Huang, X.; Ghosh, S.; Duong, T.; Karaman, I.; Elwany, A.; Arróyave, R. Finite interface dissipation phase field modeling of Ni–Nb under additive manufacturing conditions. Acta Materialia 2020, 185, 320-339. doi.org/10.1016/j.actamat.2019.11.057
24. Kim, S. G.; Kim, W. T.; Suzuki, T. Phase-field model for binary alloys. Physical Review. E, Statistical Physics, Plasmas, Fluids, and Related Interdisciplinary Topics 1999, 60, 7186-7197. doi.org/10.1103/PhysRevE.60.7186
25. Zhang, L.; Stratmann, M.; Du, Y.; Sundman, B.; Steinbach, I. Incorporating the CALPHAD sublattice approach of ordering into the phase-field model with finite interface dissipation. Acta Materialia 2015, 88, 156-169. doi.org/10.1016/j.actamat.2014.11.037
26. Steinbach, I. Phase-field models in materials science. Modelling and Simulation in Materials Science and Engineering 2009, 17, (31pp).
27. Nomoto, S.; Wakameda, H.; Segawa, M.; Yamanaka, A.; Koyama, T. Solidification analysis by non-equilibrium phase field model using thermodynamics data estimated by machine learning. Modelling and Simulation in Materials Science and Engineering 2019, 27, (15pp). doi.org/10.1088/1361-651X/ab3379
28. Kobayashi, R. Modeling and numerical simulations of dendritic crystal growth. Physica D 1993, 63, 410-423
29. (Accessed on 1 February 2021)
30. (Accessed on 1 February 2021)
31. (Accessed on 1 February 2021)

---

32. Prasad, A.; Yuan, L.; Lee, P.; Patel, M.; Qiu, D.; Easton, M.; StJohn, D. Towards understanding grain nucleation under Additive Manufacturing solidification conditions. Acta Materialia 2020, 195, 392-403. doi.org/10.1016/j.actamat.2020.05.012
33. Kurz, W.; Fisher, D. J. Appendix 6 Thermodynamics of rapid solidification. In Fundamentals of Solidification,4th ed.; Trans Tech Publications Ltd: Zürich, Switzerland Location, 1998; pp. 220-225
34. Segawa, M.; Yamanaka, A.; Nomoto, S. Multi-phase-field simulation of cyclic phase transformation in Fe-C-Mn and Fe-C-Mn-Si alloys. Computational Materials Science 2017, 136, 67-75. doi.org/10.1016/j.commatsci.2017.04.014
35. Kurz, W.; Fisher, D. J. Chapter four: Solidification microstructure: Cells and dendrite. In Fundamentals of Solidification,4th ed.; Trans Tech Publications Ltd: Zürich, Switzerland Location, 1998; pp. 63-88
36. Kusano, M.; Kitano, H.; Watanabe, M. Novel calibration strategy for validation of finite element thermal analysis of selective laser melting process using Bayesian optimization. Additive Manufacturing Reviewed